Article

Comparative and Efficient Ammonia Gas Sensing Study with Self-assembly-Synthesized Metal Oxide-SiC Fiber-Based Mesoporous SiO$_2$ Composites

Md Nazmodduha Rafat, Young Jun Joo, Kwang Youn Cho, Sang Yul Park, Kwang Youl Park, and Won-Chun Oh*

Read Online

ACCESS | Metrics & More | Article Recommendations

ABSTRACT: Self-assembled-assisted ternary nanocomposite In$_2$O$_3$−SiC, CuO$_2$−SiC, and MnO$_2$−SiC semiconductors were mixed with SiO$_2$ to enable gas sensing using cyclic voltammetry. The results of TEM (transm In$_2$O$_3$−SiC−SiO$_2$ ion electron microscopy), X-ray diffraction spectroscopy, and Raman spectra analysis affirm the closeness of few layers between SiO$_2$ and SiC in In$_2$O$_3$−SiC, MnO$_2$−SiC, and CuO$_2$−SiC. Among the electrochemical impedance spectra curves of the nanocomposites, none of the samples had a semicircle profile, which indicates the existence of a higher charge-transfer resistivity behavior between the electrolyte and the sample electrode with charge carrier and transport effects, which is related to the well-developed porous structure of synthesized composites. CuO$_2$−SiC−SiO$_2$ and MnO$_2$−SiC−SiO$_2$ showed high resistivity and a quite significant response for NH$_3$ gas at room temperature. While there was a response for NH$_3$ gas for In$_2$O$_3$−SiC−SiO$_2$, the sensor showed a low response for the gas. From the sensing test, correspondences between the chemical structure of the sensor and the molecular structure of the gases have been found. The surface reactions between the sensor surface and the gas with a pore structure, along with the electron receiver/donor phase are observed from the results of gas sensor tests, and all factors are determining the precise state. Finally, the adsorption of NH$_3$ molecules and the alteration of the electronic resistance of In$_2$O$_3$−SiC−SiO$_2$, MnO$_2$−SiC−SiO$_2$, and CuO$_2$−SiC−SiO$_2$ were presented that include various thicknesses of charge to represent which are achieved by the connection with the substrates and the particles.

Gas sensing Mechanism with Metal Oxide-SiC Fiber based Mesoporous SiO₂ Composites
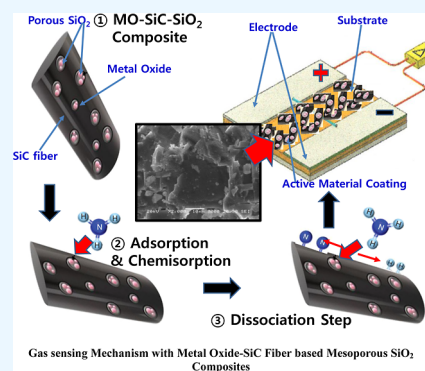
1. INTRODUCTION

Although various applications of SiC fibers were fabricated, various significant methods need to be examined. Due to continued increase in human population, more and more industrial toxic gases—such as CO, CO$_2$, NO, NO$_2$, NH$_3$, SO$_2$, H$_2$S, and volatile organic compounds—are discharged to the environment. Figuring out such gases is an important aspect of ensuring human health. Many sensors have been made to detect these toxic gases, including electrochemical sensors, biosensors, surface acoustic wave sensors, and immunosensors, and among them, chemiresistive sensors have been developed as one of the most common established sensors due to their simplicity, rapid response, and low-cost of procurement.[1−5] The adsorption capacity of NH$_3$ increased while the NH$_3$ and O$_2$ mixture increased. To explain the sensing mechanism of unfunctionalized SiC-based composites, synergistic adsorption was used, where abundant unoccupied active sites can capture more gases. It could lead to higher adsorption capacity compared to the single components.

Sensing the toxic and harmful gases from the environment has received extensive attention in recent years.[6−13] NH$_3$ and NO$_2$ are typical environmental pollution gases, and the effective detection of such gases is becoming increasingly urgent.[14−18] SiC-based composites have recently been developed as an effective candidate for next decade room-temperature NH$_3$ gas sensors. However, the surface-active sites of two-dimensional porous composites are mainly concentrated at the edge of lamella, while the content of active sites on the base plane is reduced,[19−21] thus resulting in low NH$_3$ sensing response at room temperature. SiC-based gas sensors also have the problems of poor recovery ability, poor selectivity, and stability at room temperature. Therefore, the NH$_3$ sensing performance of SiC-based gas sensors at room temperature is still far from the theoretical value and practical applicability. High-temperature assistance has proven to be an effective method for improving the NH$_3$ sensing performance

of SiC fiber-based composites.[22−27] Some reports have shown that high-temperature assistance could substantially improve the recovery speed of metal oxide-SiC-based NH_3 gas sensors.[28] The results of a mechanism study showed that high-temperature assistance and polymer base could change the number of surface-active centers,[29−33] which was the key to improving the gas sensing performance of semiconductors at high temperature and polymer-based affinity.[34] However, to recombine in pure metal oxides, implemented temperature is an easy step, which results in a limited number of NH_4^+ and O_2^- and contributes to the gas sensing reaction. Therefore, the gas sensing performance of pure metal oxides is still unsatisfactory, even under the condition of low-temperature assistance. To solve these problems, the porosity of the base material is important for increasing the gas sensing effect. Moreover, semiconductor-based heterojunctions have been modified to sense traditional metal oxide gas sensing materials on the surface of SiO_2, which is an attractive method for improving its high-temperature gas sensing performance.[35−38] On the one hand, the large specific surface characteristics of 2D In_2O_3−SiC−SiO_2, MnO_2−SiC−SiO_2, and CuO_2−SiC−SiO_2 nanocomposites provide significant supports for oxide nanocrystals and improve the use of sensitive bodies. Moreover, it is assumed that the recombination of electrons and holes could be prevented to a certain extent through the effect of the built-in electric field in heterojunctions. Studies have shown that the surface fabrication of SiO_2 can improve the response and stability of pure metal oxides active materials in the detection of NH_3 at high temperatures.[39−43]

However, overall, there are still few studies examining the room-temperature gas sensing heterojunctions under high-temperature assistance. The relationship between the surface/interface structure of heterojunctions and their gas adsorption activity/interface charge transfer behavior to this point is still unclear. The high-temperature gas sensing mechanism also needs to be studied. In fact, because of the weak interface interaction and mismatch of energy band structure, it is often hard to form effective heterojunctions between SiO_2 and metal oxides,[44−46] which makes it hard to achieve significant separation of hole−electron carriers at the interface. Therefore, the charge signal of the gas sensing reaction cannot be efficiently converted into resistance signal, which prevents any further development of the room-temperature gas sensing performance of In_2O_3−SiC−SiO_2, MnO_2−SiC−SiO_2, and CuO_2−SiC−SiO_2 metal oxide heterojunctions.

2. EXPERIMENTAL SECTION

2.1. Materials. Copper(II) sulfate pentahydrate ($CuSO_4$·$5H_2O$) has been obtained from Duksan Pure Chemicals Co. Ltd., Korea. Manganese(II) chloride tetrahydrate $MnCl_2$·$4H_2O$ and indium(III) oxide In_2O_3 have been purchased from Sigma-Aldrich Co. Ltd. Triblock copolymer Pluronic F-127, hydrochloric acid (99%) HCl, tetraethyl orthosilicate (TEOS), ethanol 98%, and SiC fiber have also been purchased. Commercial grade chemicals were purchased and used without further purification.

2.2. Synthesis of Mesoporous SiO_2. To begin, 1.1 g of triblock copolymer Pluronic F-127 was consolidated to 15 mL of deionized water containing 2 M HCl at 40 °C. Then, it is required to mix until the copolymer was completely broken down. After that, 3.20 g of TEOS was drowned and blended at 40 °C for 12.5 h. The mixture was transferred to a fixed holder and warmed to 100 °C in a dry oven for 20 h. Then, it was

sifted and washed with water and ethanol. In the next step, it is needed to dry at 65 °C for a short amount of time. Finally, the copolymer was cleared by calcination in air at 550 °C for 3 h.

2.3. Synthesis of In_2O_3−SiC−SiO_2, MnO_2−SiC−SiO_2, and CuO_2−SiC−SiO_2. First, three different solutions have been prepared with deionized (DI) water, which contain Cu, In, and Mn containing precursor. 1 mol of copper(II) sulfate pentahydrate has been stirred with 40 mL of DI water. Next, 1.0 g of SiC powder has been treated with 20 mL of ethanol. Then, both the solutions have been mixed via stirring. The temperature condition was 40−60 °C. We followed this condition until the water vaporized. This paste has been marked as solution A. Then, we added mesoporous SiO_2 in this paste. The previously prepared 1.0 g of the SiO_2 sample was supposed to be treated with 40 mL of ethanol and 60 mL of DI water. Then, this solution needed to have paste solution A added to it. After stirring for 30 min, the solution was transferred in 100 mL Teflon to a stainless-steel autoclave machine, and the hydrothermal process was followed for 5 h at 120 °C. Next, the solution was washed with DI water several times and dried at 60 °C for 3 h. Then, it had to be calcined at 600 °C for 3 h. The collected sample was marked as CuO_2−SiC−SiO_2. The same experimental conditions have been applied to prepare the In_2O_3−SiC−SiO_2 and MnO_2−SiC−SiO_2 samples, where the manganese(II) chloride tetrahydrate and indium(III) oxide amounts were 1 mol.

2.4. Characterization. The structural morphology of crystals of the product were analyzed by powder X-ray powder diffraction (XRD; Rigaku, X-beam Diffractometer) with Cu $K\alpha$ radiation (λ = 1.5406 A) at 40 kV and 30 mA over a 2θ range of (20−70)°. The prepared sample powder for XRD analysis was acquired using the General Structure Analysis System (GSAS, A.C. Larson and R.B. Von Dreele, Los Alamos National Laboratory). The organization of the as-integrated product was investigated using vitality dispersive X-beam spectrometry (JSM-76710F, JEOL, Tokyo, Japan). Filtering electron microscopy (SEM JOEL 6701, JEOL Ltd, Tokyo, Japan) has been used to clarify the morphology of the images. The size and the morphology of the high-resolution transm In_2O_3−SiC−SiO_2 ion electron microscopy (TEM) were examined by using transmission electron microscopy (TEM; JSM-76710F, JEOL, Tokyo, Japan) at a 300 kV excitation voltage. Electrochemical impedance spectra (EIS, using an electrochemical analyzer, Zahner, Germany) has been used to carry out the resistivity of the sample. Nitrogen adsorption/desorption isotherms were analyzed by Micro Active for ASAP 2460, and the pore size distribution was figured out according to the Barrett−Joyner−Halenda method. X-ray photoelectron spectroscopy analysis was performed using electron spectrometry (WITec alpha 300 arrangement). The current−voltage (I−V) were recorded using a PG201 (Potentiostat, Galvanostat, VoltaLab, Radiometer, Copenhagen) in a protected and clean box at RT.

2.5. Electrical Performance Test. Cyclic voltammetry (CV) and estimations were performed under a two-electrode electrochemical arrangement to examine the current and voltage profiles, and this arrangement used In_2O_3−SiC−SiO_2, MnO_2−SiC−SiO_2, and CuO_2−SiC−SiO_2 as working electrodes. Here, a working electrode has been used as a cathode and anode electrode. The working electrode is 2.5 × 2.5 cm^2, which was coated on nickel foam. For this measurement, the sample electrode was placed in a tube-type chamber to measure the gas sensor capacity, and at this time, ammonia gas sensing

performance was measured under conditions with constant temperature and humidity.

3. RESULTS AND DISCUSSION

XRD patterns show the crystal phase information of the different samples, which are shown in Figure 1. It can be seen
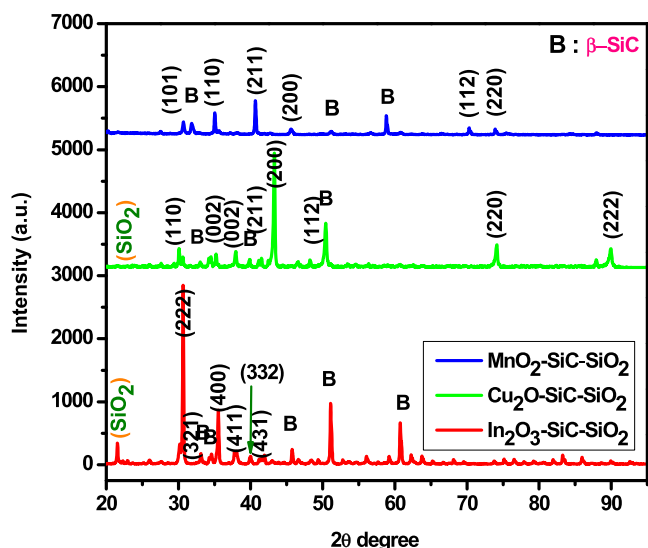

Figure 1. XRD patterns of $In_2O_3-SiC-SiO_2$, $Cu_2O-SiC-SiO_2$, and $MnO_2-SiC-SiO_2$.

that $In_2O_3-SiC-SiO_2$, $MnO_2-SiC-SiO_2$, and $Cu_2O-SiC-SiO_2$ samples show typical diffraction peaks of In_2O_3-SiC, MnO_2-SiC, CuO_2-SiC, and SiO_2. The XRD patterns of $In_2O_3-SiC-SiO_2$, $MnO_2-SiC-SiO_2$, and $CuO_2-SiC-SiO_2$ show mixed phases of hexagonal In_2O_3-SiC, MnO_2-SiC,

CuO_2-SiC, and SiO_2.[47,48] The diffraction peaks of hexagonal In_2O_3-SiC, MnO_2-SiC, and CuO_2-SiC are relatively weak due to the two-dimensional lamellar structure, and the strong diffraction peak of SiO_2 nanocrystals masks it to a great extent. Based on the XRD data, three types of samples as an active material form a distinct crystal structure, which is believed to have an effect of maximizing the sensor effect. In particular, the distinct SiO_2 crystal structure is believed to increase the ammonia reactivity.

Figure 2 shows the structural morphology and elemental information of the three samples. As can be seen from Figure 2a−c, there is a typical two-dimensional lamellar structure, and the nanocomposites are intertwined to form a rodlike structure. It can be seen that metal oxides and SiO_2 compounds are uniformly distributed around rodlike SiC. These results show that rodlike SiC can play an important role as a substrate material, and that it may play a central role in localization and reactivity with metal oxides and SiO_2 compounds in the formation of nanocomposites. This can clearly be seen from Figure 2a−c. The energy-dispersive X-ray spectroscopy (EDS) spectra show the presence of In, Cu, Mn, Si, C, and O in the $In_2O_3-SiC-SiO_2$, $MnO_2-SiC-SiO_2$, and $CuO_2-SiC-SiO_2$. The higher amount of O indicates high oxidation in composites.

It can clearly be seen in the TEM images in Figure 3a,c,e that the nanocomposites are well aggregated. The spacing of the (222,002,110) crystal facets of typical hexagonal $In_2O_3-SiC-SiO_2$, $MnO_2-SiC-SiO_2$, and $CuO_2-SiC-SiO_2$, respectively, can clearly be shown in the high-resolution TEM (HRTEM) image, as shown in Figure 3b,d,f. TEM images clearly show that excellent heterogeneous interface contact is formed between In_2O_3-SiC, MnO_2-SiC, CuO_2-SiC nanocomposites, and SiO_2 nanocrystals, as can be found in Figure 3a,c,e, which is a key aspect of the effective charge transfer
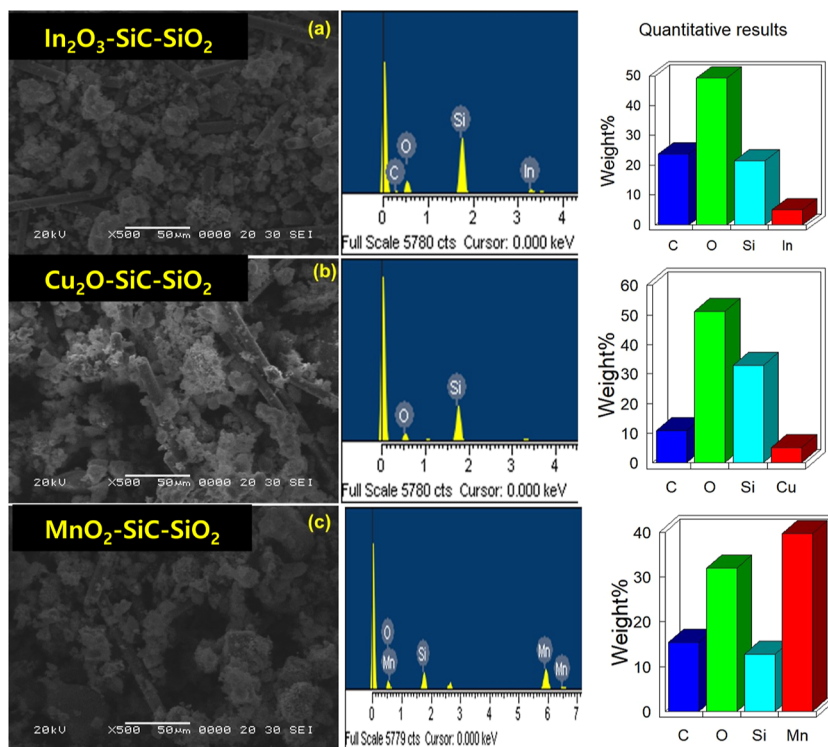

Figure 2. SEM images and EDS of (a) $In_2O_3-SiC-SiO_2$, (b) $Cu_2O-SiC-SiO_2$, and (c) $MnO_2-SiC-SiO_2$.
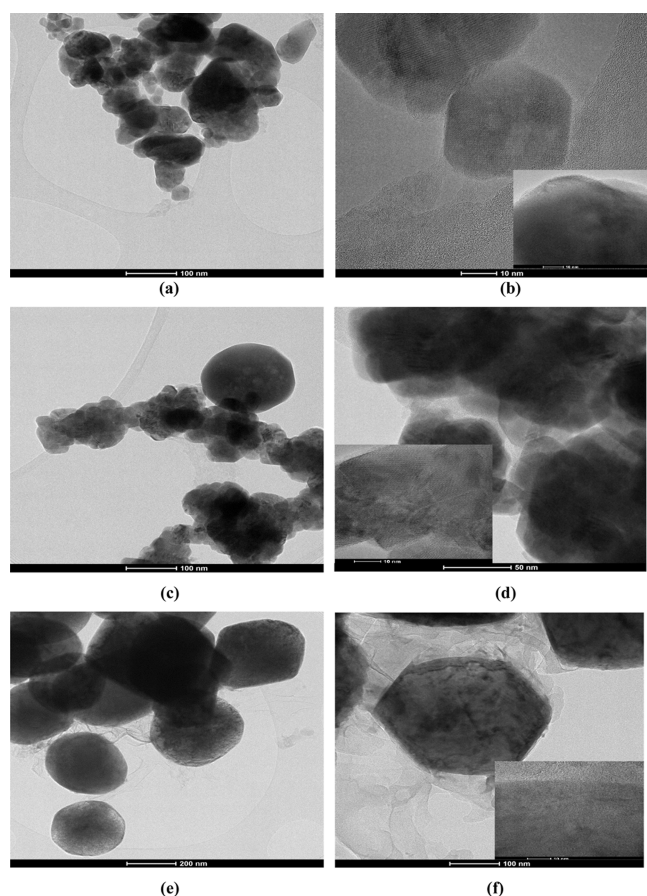
Figure 3. TEM and HRTEM images: (a,b) $In_2O_3-SiC-SiO_2$, (c,d) $CuO_2-SiC-SiO_2$, and (e,f) $MnO_2-SiC-SiO_2$.

between heterojunctions. Furthermore, using a simple self-assembled method, we have synthesized $In_2O_3-SiC-SiO_2$, $MnO_2-SiC-SiO_2$, and $CuO_2-SiC-SiO_2$ heterojunction materials with clear crystal facet exposure, which provides an ideal model for studying the structure–activity relationship between the surface/interface and the properties of heterojunction materials.

Furthermore, the Raman spectra of the $In_2O_3-SiC-SiO_2$, $MnO_2-SiC-SiO_2$, and $CuO_2-SiC-SiO_2$ nanocomposites with various G contents, as shown in Figure 4, reveal that
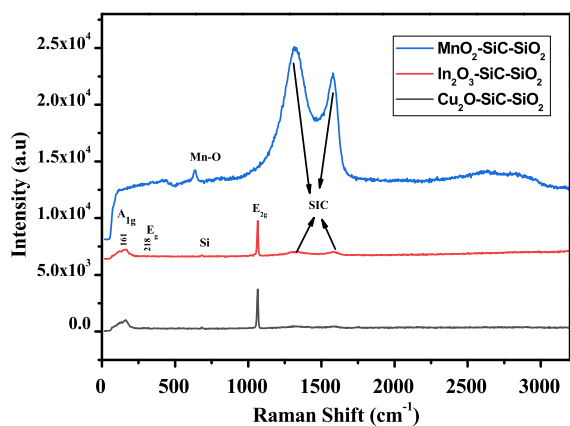

Figure 4. Raman spectra of $In_2O_3-SiC-SiO_2$, $MnO_2-SiC-SiO_2$, and $CuO_2-SiC-SiO_2$.

SiC had a spectral peak of about 1354 cm^{-1}, which was attributable to the D band associated with the nano-auxiliary deformities of carbon spaces and generated by interactions in the carbon plane. The crests at 1569, 1577, and 1585 cm^{-1} are related to the G band, which results from the main distribution of the phonon E_{2g} of the C sp2 molecules.[49,50] As a rule, a G-band configuration involves a charge exchange, which produces a range of graphene electrical properties. Shifts in the red G band can be seen with a greater measure of G, which declared the arrangement of new areas of carbon during heat treatment. Meanwhile, the decreased strength of the D/G ratio confirmed a slight low peak in G, which then made greater carbon crystallinity by constantly increasing the G. For the compound $In_2O_3-SiC-SiO_2$, $MnO_2-SiC-SiO_2$, and $CuO_2-SiC-SiO_2$, the groups D and G expanded and decreased significantly. The downward change in the G band has been ascribed to the incomplete interaction of the metal particles, thus suggesting that the nanocrystals bond weakly to the carbon. These results suggest that the nanocomposite represented a channel for transporters and the prevailing electrical and charge-sharing properties.[51,52]

Figure 5 shows the EIS spectroscopy results of the $In_2O_3-SiC-SiO_2$, $MnO_2-SiC-SiO_2$, and $CuO_2-SiC-SiO_2$ samples.
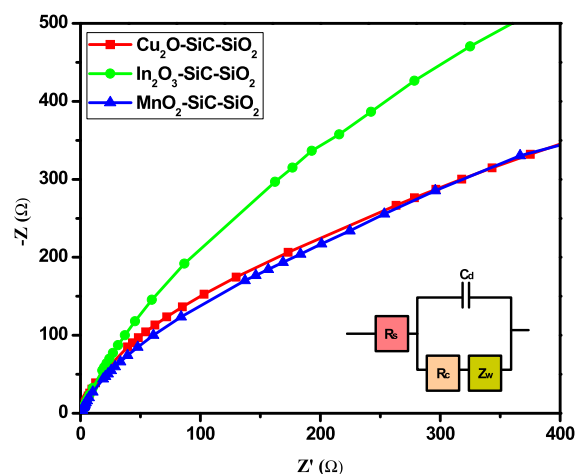
Figure 5. Nyquist plots of $In_2O_3-SiC-SiO_2$, $MnO_2-SiC-SiO_2$, and $CuO_2-SiC-SiO_2$ samples.

It can clearly be seen that those samples have high resistivity. Compared to $In_2O_3-SiC-SiO_2$ and $CuO_2-SiC-SiO_2$ samples, the $MnO_2-SiC-SiO_2$ composite has shown low resistivity. Thus, the $MnO_2-SiC-SiO_2$ sample has large electron-transfer carrier. Among the EIS curves of the nanocomposites, none of the samples had a semicircle profile, which indicates the existence of a higher charge-transfer resistance between the sample electrode and the electrolyte with charge carrier and transport effects. Further analysis has been conducted to show the porous structure of the synthesized composites. From Figure 6a, it is apparent that the $MnO_2-SiC-SiO_2$ sample has a high nitrogen absorption–desorption isotherm. The $In_2O_3-SiC-SiO_2$ sample shows H1-type adsorption isothermal curves, and this hysteresis curve does not show a percolation effect due to the metastable pore fluid and the narrow pore-size distribution. On the other hand, $CuO_2-SiC-SiO_2$ and $MnO_2-SiC-SiO_2$ show H2-type adsorption isothermal curves. It is considered that their hysteresis curves show the pore fluid and percolation effect
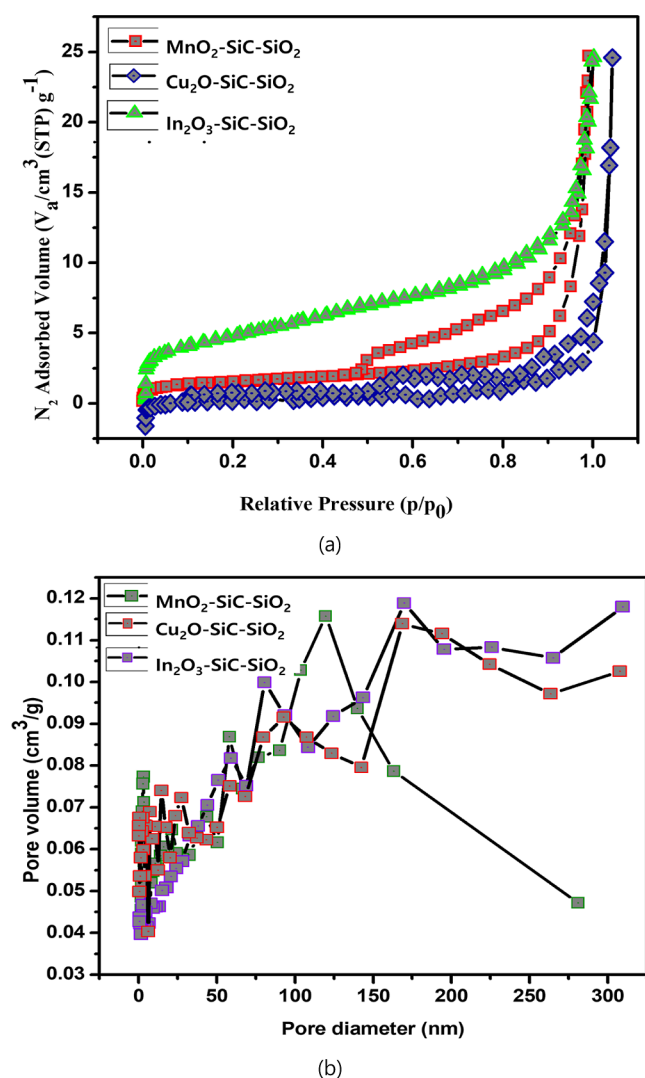
Figure 6. (a) Nitrogen adsorption–desorption isotherms and (b) pore distribution of In_2O_3–SiC–SiO$_2$, MnO_2–SiC–SiO$_2$, and CuO_2–SiC–SiO$_2$ sample.

due to the presence of both metastable states and broad pore-size distribution. However, CuO_2–SiC–SiO$_2$ and In_2O_3–SiC–SiO$_2$ composites have a small loop between the 0.2 and 0.8 cm^2/g region, whereas the MnO_2–SiC–SiO$_2$ sample shows bigger hysteresis loops than the others. Thus, the MnO_2–SiC–SiO$_2$ sample has a small pore diameter, and the sample will show a larger light absorption effect. In the pore size distribution results, it can be seen that the MnO_2–SiC–SiO$_2$ sample contains larger pore levels than the In_2O_3–SiC–SiO$_2$ and CuO_2–SiC–SiO$_2$ samples, as shown in Figure 6b. Due to the large pore volume, the MnO_2–SiC–SiO$_2$ sample has a large active surface area, which will be efficient for gas sensing.

Figure 7a–c, respectively, shows the X-ray photoelectron spectroscopy (XPS) results of the In_2O_3–SiC–SiO$_2$, MnO_2–SiC–SiO$_2$, and CuO_2–SiC–SiO$_2$ composites. XPS spectroscopy has been conducted to confirm the binding energy region of each element. It is also used to declare the presence of each element in the composite material. Figure 7a shows the binding energy survey results of the In_2O_3–SiC–SiO$_2$ sample. The binding energy of In is 463.5 eV, which is declared to be the In 3d orbital region. The presences of Si, C, and O are also observed in the In_2O_3–SiC–SiO$_2$ sample, as confirmed by the

binding energy regions at 151.89, 298.53, and 584.8 eV, respectively. In Figure 7b, the orbital positions are apparent at the Si 2p, C 1s, O 1s, and Cu 2p numbers with the binding energy regions of 101.93, 259.65, 598.41, and 998.53 eV, respectively. The binding energy region for the MnO_2–SiC–SiO$_2$ sample is shown in Figure 7c. The binding energy for Mn is 638.98 eV, and the orbital region is Mn 2p. For O, the Si 2p spectra are shown with a binding energy region of 101.59 eV. Moreover, the C 1s and O1s orbital numbers are shown in the 298.53 and 559.46 eV binding energy regions.

Figure 8 shows the ammonia gas sensing result of the In_2O_3–SiC–SiO$_2$ composite. From the CV data, it is apparent that the In_2O_3–SiC–SiO$_2$ sample exhibits constant current density results for 6 and 24 h treatment, and the current amount is around 0.8 mA cm^{-2}. On the other hand, the Cu-treated sample has a low current density result with 6 and 24 h treatment, as shown in Figure 9. Thus, further experimentation has not been applied for the CuO_2–SiC–SiO$_2$ sample. Finally, ammonia gas sensing has been tested on the MnO_2–SiC–SiO$_2$ sample with different time conditions. The Mn-treated sample showed good current density results compared to the Cu-treated sample. In Figure 10, it can be seen that the current density amount is 1.94×10^{-4} mA cm^{-2}, which is larger than that of the CuO_2–SiC–SiO$_2$ sample. Thus, it is apparent that the In_2O_3–SiC–SiO$_2$ sample will show a high sensing result. For further confirmation of the electrical response, resistance values have been calculated for In_2O_3–SiC–SiO$_2$, MnO_2–SiC–SiO$_2$, and CuO_2–SiC–SiO$_2$ composites. Figure 11 shows the resistance effect of the In_2O_3–SiC–SiO$_2$ sample for ammonia sensing as a resistance value with increasing time. The figure shows that the resistance value gradually decreases with time. It is believed that ammonia decomposes with increasing time or that the ammonia adsorption properties decrease on the sample surface.

Figure 11 also shows the resistance effect of CuO_2–SiC–SiO$_2$ on ammonia sensing as a resistance value for a function of time. It can be seen that the resistance value gradually increases with increasing time. It appears that the resistance value increases due to the accumulation of the adsorption amount of ammonia with increasing time, and it is believed that the ammonia adsorption reactivity on the sample surface is increased. In addition, due to the increase in porosity, many ammonia molecules are continuously filled in the pores, and the adsorption amount is increasing as a result. The resistance effect of MnO_2–SiC–SiO$_2$ on ammonia sensing as a resistance value as a function of time is presented in Figure 11. At the initial step, the resistance value is shown to increase slowly and gradually. However, with increasing time, the resistance value shows a tendency to rapidly increase. This indicates that the adsorption amount of ammonia is not very large in the initial time, and the adsorption amount shows a rapid increase with increasing time, which is correlated with the increase in resistance value. In addition, due to the increase in porosity, many ammonia molecules are continuously stacked in the pores, and the adsorption amount is therefore increasing. This is inefficient for initial sensing effects, but devices requiring long-term sensing effects are expected to show excellent efficiency. Thus, the CuO_2–SiC–SiO$_2$ sample will show higher sensing response than other synthesized samples. These redox peaks in the curve could be due to the immediate electron-transfer behaviors of In_2O_3–SiC–SiO$_2$, MnO_2–SiC–SiO$_2$, and CuO_2–SiC–SiO$_2$. Here, all samples show small redox curves, and CuO_2–SiC–SiO$_2$ composites show smaller redox curves
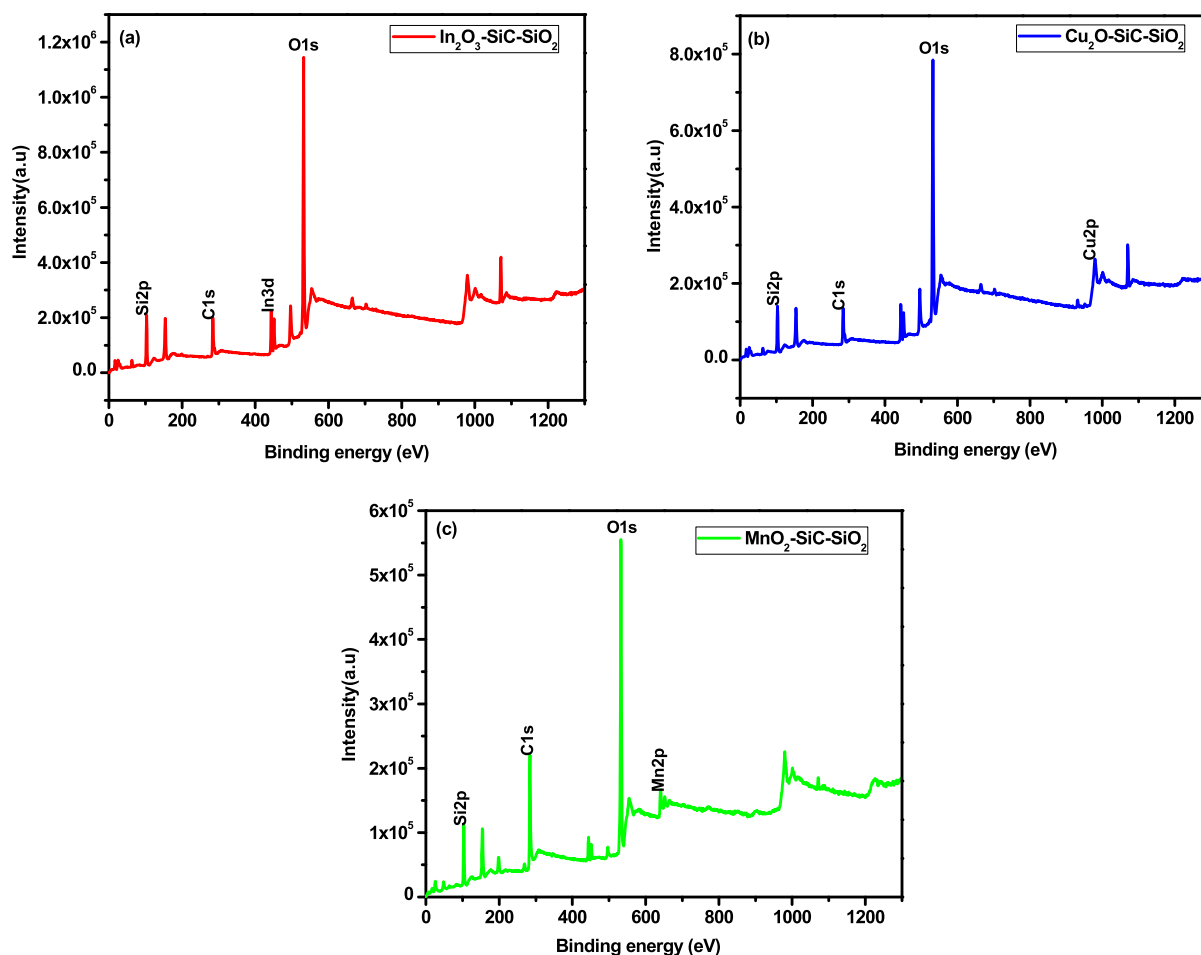
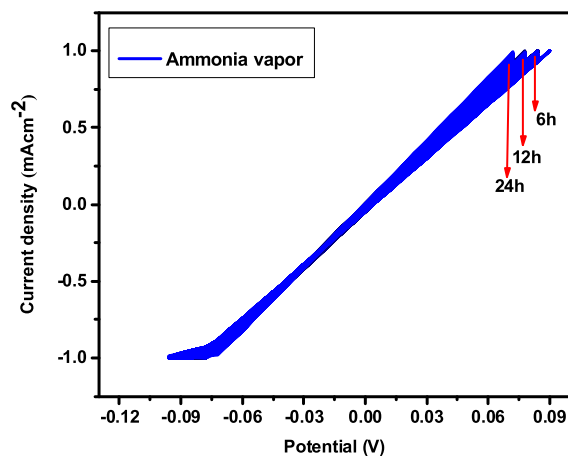**Figure 7.** XPS spectra of (a) In_2O_3−SiC−SiO$_2$, (b) CuO_2−SiC−SiO$_2$, and (c) MnO_2−SiC−SiO$_2$ survey.

Figure 8. Ammonia sensing effects with In_2O_3−SiC−SiO$_2$ as active material for 6−24 h.
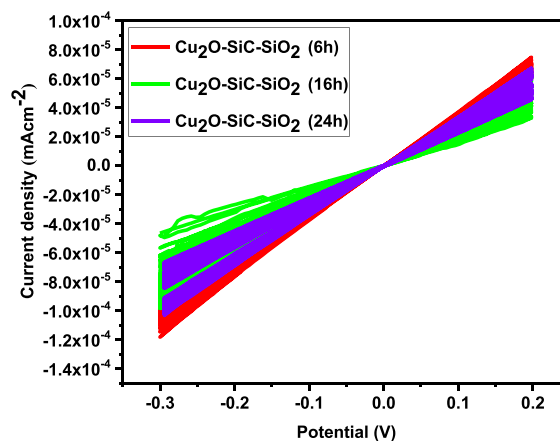
Figure 9. Ammonia sensing effects with Cu_2O−SiC−SiO$_2$ as active material for 6−24 h.

than In_2O_3−SiC−SiO$_2$, and MnO_2−SiC−SiO$_2$ thus indicating high resistivity. The presence of NH_3 gas has prevented hole to electron generation.[53] The sensing mechanism also rely on the charge-transfer process based on oxidation and reducing the behavior of the target gas, and also regarding the atomic surface of the nanostructures.[54,55] In the present study, bare In_2O_3−SiC, MnO_2−SiC, and CuO_2−SiC are amalgamated with SiO_2, which can demonstrate a reduction in electrical noise and a constant enhancement in current conduction.

However, there is a low electron generation presence of NH_3, thus leading to a low redox reaction.[56]

To assess the concentration-dependent electrochemical reactions of In_2O_3−SiC−SiO$_2$, MnO_2−SiC−SiO$_2$, and CuO_2−SiC−SiO$_2$ samples under different concentrations of NH_3 gas, as shown in Figure 12, we recorded it at a connected potential of 0.2 V. A stepwise increment in current density was observed upon the expansion of ammonia gas at increasing concentrations. The In_2O_3−SiC−SiO$_2$ sample exhibited a high
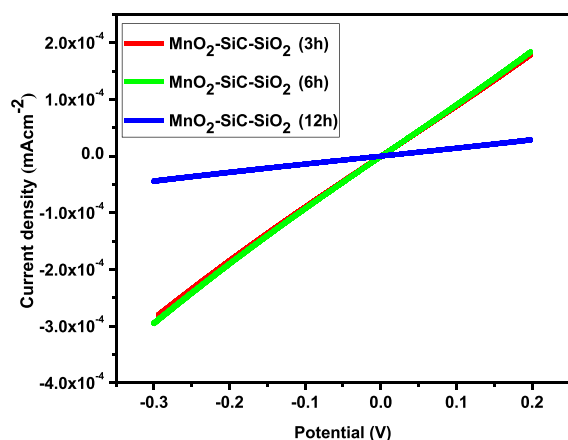
Figure 10. Ammonia sensing effects with $MnO_2-SiC-SiO_2$ as active material for 3−12 h.

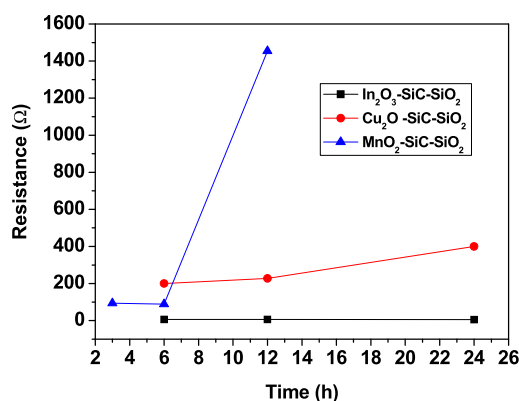**Figure 11.** Resistance values with time condition of $In_2O_3-SiC-SiO_2$, $Cu_2O-SiC-SiO_2$, and $MnO_2-SiC-SiO_2$ with ammonia.
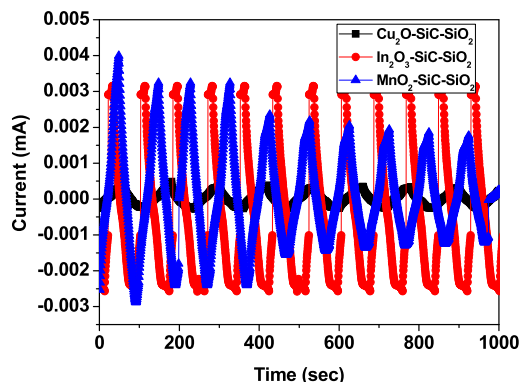

Figure 12. Current variation under different NH_3 concentrations (0.1−1.0 mL/s).

current value in the whole range along with an increase in concentrations, and it maintained a constant current value. The $MnO_2-SiC-SiO_2$ sample showed a high current value from the initial concentration value, and as the time and concentration increased, the current value showed a tendency to slowly decrease. The $CuO_2-SiC-SiO_2$ sample maintained a low current value throughout the whole range, and it showed a tendency to maintain a constant current value along with increasing time and concentration. Among the three types of samples, $CuO_2-SiC-SiO_2$ showed a stable sensing effect, while $MnO_2-SiC-SiO_2$ showed a gradually stable sensing

effect. Therefore, $MnO_2-SiC-SiO_2$ is expected to show excellent characteristics when measuring sensor effects for a long period of time. Interestingly, we observed an enhancement in the sensing effect within the greatness of the standard deviation in moving toward higher ammonia concentrations, which may correspond to an increase in the sensing effect within the inconstancy of detection as the samples approached the upper concentration limit of ammonia. The sensor effect has multiple variables, and it is correlated with the conductivity of the constituent element and the compound, the adsorption characteristics due to porosity, and the gas reactivity. Here, one can see that the response range corresponds to the concentration extent. After observing this proportion that can effortlessly reach to this choice that able to degree of ammonia gas sensing test with this sensor for subjective and quantitative analysis.[56,57]

Furthermore, Scheme 1 depicts a mechanism showing the working material preparation and their working principal. It is

Scheme 1. NH_3 Adsorption and Chemisorption Mechanisms and Design of Electrodes for the Electrical Performance Test
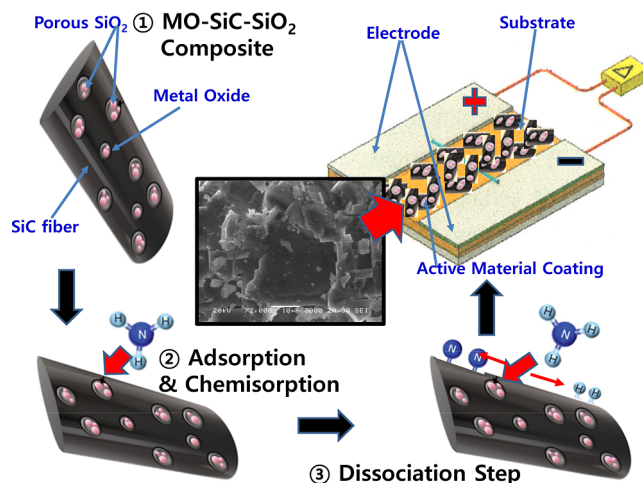
apparent that the active materials have been coated on the surface of nickel foam. Generally, an active material produced hole−electron and transfer electron from the valance band to the conduction band. As the samples have a mesoporous structure and as metallic In_2O_3-SiC, MnO_2-SiC, and CuO_2-SiC have been added on the surface of mesoporous SiO_2, samples have active surface area containing pores. Although the samples also have semiconductive behavior, the presence of NH_4^+ prevented electron production by blocking active pores and increasing the resistive active surface. Thus, these samples will show high resistivity at room temperature and high temperature. This experimental condition declared the gas sensing efficiency of the sample NH_3.[53,57,58] The fibrous base materials used so far have good conductivity and durability, but they lack pore and gas affinity.[59,60] Therefore, in this study, fibrous SiCs with good properties were used to form complex SiO_2 with porosity and a metal oxide with gas affinity.

4. CONCLUSIONS

In summary, $In_2O_3-SiC-SiO_2$, $MnO_2-SiC-SiO_2$, and $CuO_2-SiC-SiO_2$ composites were prepared through a self-assembled method on the SiC fiber surface. The room-temperature NH_3 sensing properties of the heterojunctions

were studied under low-temperature assistance. It was found that $CuO_2-SiC-SiO_2$ and $MnO_2-SiC-SiO_2$ heterojunctions showed a significantly higher sensing response than $In_2O_3-SiC-SiO_2$ composites, thus suggesting a strong synergistic effect. The high gas sensing performance of the heterojunction can also be related to adsorption capacity with pore structure and porosity for NH_3 gas. Current density was obtained from $I-V$ curves and EIS spectra to clarify the gas sensing behavior. The gas sensing test found a correlation between the molecule structure, the electron donor/acceptor phase of the gases, and the chemical structure of the sensor. The estimations have been presented to include various thicknesses of charge to represent the adsorption of NH_3 molecules, and the alteration of the electronic resistance of $In_2O_3-SiC-SiO_2$, $MnO_2-SiC-SiO_2$, and $CuO_2-SiC-SiO_2$ was achieved by the connection with the substrates and the particles. The results provide a new model through which to improve the room-temperature-assisted gas sensing performance of SiC-based gas porous sensors through the construction of porous heterojunctions, which will essentially increase the development of NH_3 gas sensors.

■ AUTHOR INFORMATION

Corresponding Author

Won-Chun Oh − *Department of Advanced Materials Science & Engineering, Hanseo University, Seosan-si 356-706, Korea; College of Materials Science and Engineering, Anhui University of Science & Technology, Huainan 232001, P. R. China;* ● orcid.org/0000-0002-0154-7388; Phone: +82-41-660-1337; Email: wc_oh@hanseo.ac.kr; Fax: +82-41-688-3352

Authors

Md Nazmodduha Rafat − *Department of Advanced Materials Science & Engineering, Hanseo University, Seosan-si 356-706, Korea*

Young Jun Joo − *Korea Institutes of Ceramic Engineering and Technology, Jinju-Si 52851, South Korea*

Kwang Youn Cho − *Korea Institutes of Ceramic Engineering and Technology, Jinju-Si 52851, South Korea*

Sang Yul Park − *Daeho I&T, Changwon-si 51338, Korea*

Kwang Youl Park − *Daeho I&T, Changwon-si 51338, Korea*

Complete contact information is available at:
https://pubs.acs.org/10.1021/acsomega.2c05099

Notes
The authors declare no competing financial interest.

■ ACKNOWLEDGMENTS

■ REFERENCES

(1) Joshi, S.; Lanka, S.; Ippolito, S. J.; Bhargava, S. K.; Sunkara, M. V. {111} faceted Li4Ti5O12 octahedra as the reference electrode material in a nanostructured potentiometric CO2 sensor. *J. Mater. Chem. A* **2016**, *4*, 16418−16431.

(2) Falkowski, P.; Scholes, R. J.; Boyle, E.; Canadell, J.; Canfield, D.; Elser, J.; Gruber, N.; Hibbard, K.; Högberg, P.; Linder, S.; Mackenzie, F. T.; Moore, B.; Pedersen, T.; Rosenthal, Y.; Seitzinger, S.; Smetacek, V.; Steffen, W. The global carbon cycle: a test of our knowledge of earth as a system. *Science* **2000**, *290*, 291.

(3) Soentgen, J. Hot air: the science and politics of CO2. *Glob. Environ.* **2014**, *7*, 134−171.

(4) Zheng, Y.; Huo, J.; Yang, J.; Hu, J.; Gao, J.; Wang, Q. Extensive studies of host lattices and activators in lanthanide phosphors based on efficient synthesis. *J. Alloys Compd.* **2016**, *676*, 292−298.

(5) Seppänen, O. A.; Fisk, W. J.; Mendell, M. J. Association of ventilation rates and CO2 concentrations with health andother responses in commercial and institutional buildings. *Indoor Air* **1999**, *9*, 226−252.

(6) Van Marcke, C.; Daoudia, A.; Penaloza, A.; Verschuren, F. CO2 measurement for the early differential diagnosis of pulmonary embolism-related shock at the emergency department: a case series. *Respir. Med. Case Rep.* **2015**, *16*, 106−108.

(7) Guo, Z.; Song, N. R.; Moon, J. H.; Kim, M. W.; Jun, E. J.; Choi, J.; Lee, J. Y.; Bielawski, C. W.; Sessler, J. L.; Yoon, J. A benzobisimidazolium-based fluorescent and colorimetric chemosensor for CO2. *J. Am. Chem. Soc.* **2012**, *134*, 17846−17849.

(8) Lang, T.; Hirsch, T.; Fenzl, C.; Brandl, F.; Wolfbeis, O. S. Surface plasmon resonance sensor for dIn2O3-SiC-SiO2olved and gaseous carbon dioxide. *Anal. Chem.* **2012**, *84*, 9085−9088.

(9) Lim, C.; Wang, W.; Yang, S.; Lee, K. Development of SAW-based multi-gas sensor for simultaneous detection of CO2 and NO2. *Sens. Actuators, B* **2011**, *154*, 9−16.

(10) Houk, R. J. T.; Lee, J. H.; Allendorf, M. D.; Hesketh, P. J. The metal organic films for tailorable chemical sensing on microcantilevers. *ECS Trans.* **2009**, *19*, 267−278.

(11) Djerdj, I.; Haensch, A.; Koziej, D.; Pokhrel, S.; Barsan, N.; Weimar, U.; Niederberger, M. Neodymium dioxide carbonate as a sensing layer for chemoresistive CO2 sensing. *Chem. Mater.* **2009**, *21*, 5375−5381.

(12) Joshi, S. Tailored Nanostructures for CO2 Gas Sensing Applications, Doctor of Philosophy; RMIT University, 2017.

(13) Ou, J. Z.; Ge, W.; Carey, B.; Daeneke, T.; Rotbart, A.; Shan, S.; Wang, Y.; Fu, Z.; Chrimes, A. F.; Wlodarski, W.; Russo, S. P.; Li, Y. X.; Kalantar-zadeh, K. Physiorptionbased charge transfer in two-dimensional SnS2 for selective and reversible NO2 gas sensing. *ACS Nano* **2015**, *9*, 10313−10323.

(14) Fatema, K. N.; Jung, C. H.; Liu, Y.; Sagadevan, S.; Cho, K. Y.; Oh, W. C. New design of active material based on YInWO4-G-SiO2 for a urea sensor and high performance for nonenzymatic electrical sensitivity. *ACS Biomater. Sci. Eng.* **2020**, *6*, 6981−6994.

(15) Florin, N. H.; Blamey, J.; Fennell, P. S. Synthetic CaO-based sorbent for CO2 capture from large-point sources. *Energy Fuels* **2010**, *24*, 4598−4604.

(16) Ishihara, T.; Kometani, K.; Hashida, M.; Takita, Y. Application of a mixed oxide capacitor to the selective carbon dioxide sensor. *J. Electrochem. Soc.* **1991**, *138*, 173−176.

(17) Sun, G. J.; Lee, J. K.; Choi, S. B.; Lee, W. I.; Kim, H. W.; Lee, C. M. Selective oxidizing gas sensing and dominant sensing mechanism of n-CaO-decorated n-ZnO nanorod sensors. *ACS Appl. Mater. Interfaces* **2017**, *9*, 9975−9985.

(18) Yoon, J. W.; Kim, J. S.; Kim, T. H.; Hong, Y. J.; Kang, Y. C.; Lee, J. H. A new strategy for humidity independent oxide chemiresistors: dynamic self-refreshing of In2O3 sensing surface assisted by layer-by-layer coated CeO2 nanoclusters. *Small* **2016**, *12*, 4229−4240.

(19) Boughriet, A.; Gengembre, L.; Laureyns, J.; Recourt, P.; Langelin, H. R.; Nacer, A. Generation of Uranyl/Carbonate/Hydroxide "Coatings" at the vaterite surface. *Phys. Chem. Chem. Phys.* **2000**, *2*, 1059−1068.

(20) Liu, G.; Schulmeyer, T.; Brötz, J.; Klein, A.; Jaegermann, W. Interface properties and band alignment of Cu2S/CdS thin film solar cells. *Thin Solid Films* **2003**, *431−432*, 477−482.

(21) Uddin, Md. T.; Nicolas, Y.; Olivier, C.; Jaegermann, W.; Rockstroh, N.; Junge, H.; Toupance, T. Band alignment investigations of heterostructure NiO/TiO2 nanomaterials used as efficient heterojunction earth-abundant metal oxide photocatalysts for hydrogen production. *Phys. Chem. Chem. Phys.* **2017**, *19*, 19279.

(22) Evans, D. A.; Steiner, H. J.; Vearey-Roberts, A. R.; Dhanak, V.; Cabailh, G.; O'Brien, S.; McGovern, I. T.; Braun, W.; Kampen, T. U.; Park, S.; Zahn, D. R. T. Perylenes and phthalocyanines on Gas (001) surfaces. *Appl. Surf. Sci.* **2003**, *212-213*, 417−422.

(23) Ehre, D.; Cohen, H.; Lyahovitskaya, V.; Lubomirsky, I. X-ray photoelectron spectroscopy of amorphous and quasiamorphous phases of BaTiO₃ and SrTiO₃. *Phys. Rev. B: Condens. Matter Mater. Phys.* **2008**, *77*, 184106−184112.

(24) Bolorizadeh, M. A.; Sashin, V. A.; Kheifets, A. S.; Ford, M. J. Electronic band structure of calcium oxide. *J. Electron Spectrosc. Relat. Phenom.* **2004**, *141*, 27−38.

(25) Marsal, A.; Centeno, M. A.; Odriozola, J. A.; Cornet, A.; Morante, J. R. DRIFTS analysis of the CO₂ detection mechanisms using LaOCl sensing material. *Sens. Actuators, B* **2005**, *108*, 484−489.

(26) Durán, P.; Gutierrez, D.; Tartaj, J.; Bañares, M.; Moure, C. On the formation of an oxycarbonate intermediate phase in the synthesis of BaTiO₃ from (Ba, Ti)-polymeric organic precursors. *J. Eur. Ceram. Soc.* **2002**, *22*, 797−807.

(27) Lu, S.; Leea, B.; Mann, L. Characterization of carbonate on BaTiO₃ ceramic powders mater. *Res. Bull.* **2000**, *35*, 1303−1312.

(28) Kim, P.; Jones, S. C.; Hotchkiss, P. J.; Haddock, J. N.; Kippelen, B.; Marder, S. R.; Perry, J. W. Phosphonic acid-modified barium titanate polymer nanocomposites with high permittivity and dielectric strength. *Adv. Mater.* **2007**, *19*, 1001−1005.

(29) Prim, A.; Pellicer, E.; Rossinyol, E.; Peiró, F.; Cornet, A.; Morante, J. R. A novel mesoporous CaO-Loaded In₂O₃ material for CO₂ sensing. *Adv. Funct. Mater.* **2007**, *17*, 2957−2963.

(30) Zhang, D.; Yu, S.; Wang, X.; Huang, J.; Pan, W.; Zhang, J.; Meteku, B. E.; Zeng, J. UV illumination-enhanced ultrasensitive ammonia gas sensor based on (001)TiO₂/MXene heterostructure for food spoilage detection. *J. Hazard. Mater.* **2022**, *423*, 127160.

(31) Zhang, D.; Yang, Y.; Xu, Z.; Wang, D.; Du, C. An eco-friendly gelatin based triboelectric nanogenerator for a self-powered PANI nanorod/NiCo2O4nanosphere ammonia gas sensor. *J. Mater. Chem.A* **2022**, *10*, 10935−10949.

(32) Otgonbayar, Z.; Joo, Y. J.; Cho, K. Y.; Park, S. Y.; Park, K. Y.; Oh, W. C. Novel synthesis of ternary nanocomposites with b-SiC fibers, SnO2, and In2O3 for atmospheric gas sensing under high temperature conditions. *J. Mater. Chem. C* **2022**, *10*, 12106.

(33) Wang, X.; Zhang, D.; Zhang, H.; Gong, L.; Yang, Y.; Zhao, W.; Yu, S.; Yin, Y.; Sun, D. In situ polymerized polyaniline/MXene (V2C) as building blocks of supercapacitor and ammonia sensor self-powered by electromagnetic-triboelectric hybrid generator. *Nano Energy* **2021**, *88*, 106242.

(34) Yin, Y.; Zhang, H.; Huang, P.; Xiang, C.; Zou, Y.; Xu, F.; Sun, L. Inducement of nanoscale Cu−BTC on nanocomposite of PPy−rGO and its performance in ammonia sensing. *Mater. Res. Bull.* **2018**, *99*, 152−160.

(35) Liu, C.; Ma, Q.; Liu, Y.; Ma, J.; He, H. Synergistic reaction between SO₂ and NO₂ on mineral oxides: a potential formation pathway of sulfate aerosol. *Phys. Chem. Chem. Phys.* **2012**, *14*, 1668−1676.

(36) Roso, S.; Degler, D.; Llobet, E.; Barsan, N.; Urakawa, A. Temperature-dependent NO₂ sensing mechanism over indium oxide. *ACS Sens.* **2017**, *2*, 1272−1277.

(37) Keller, P.; Ferkel, H.; Zweiacker, K.; Naser, J.; Meyer, J. U.; Riehemann, W. The application of nanocrystalline BaTiO₃ composite films as CO₂ sensing layers. *Sens. Actuators, B* **1999**, *57*, 39−46.

(38) Liao, B.; Wei, Q.; Wang, K.; Liu, Y. Study on CuO−BaTiO₃ semiconductor CO₂ sensor. *Sens. Actuators, B* **2001**, *80*, 208−214.

(39) Biswas, M. R. U. D.; Oh, W. C. Comparative study on gas sensing by a Schottky diode electrode prepared with graphene−semiconductor−polymer nanocomposites. *RSC Adv.* **2019**, *9*, 11484−11492.

(40) El-Sayed, A. M.; Ismail, F. M.; Yakout, S. M. Electrical conductivity and sensitive characteristics of Ag added BaTiO₃-CuO mixed oxide for CO₂ gas sensing. *J. Mater. Sci. Technol.* **2011**, *27*, 35−40.

(41) Herrán, J.; Mandayo, G. G.; Pérez, N.; Castaño, E.; Prim, A.; Pellicer, E.; Andreu, T.; Peiró, F.; Cornet, A.; Morante, J. R. On the structural characterization of BaTiO₃−CuO as CO₂ sensing material. *Sens. Actuators, B* **2008**, *133*, 315−320.

(42) Herrán, J.; Fernández-González, O.; Castro-Hurtado, I.; Romero, T.; Mandayo, G. G.; Castaño, E. Photoactivated solid state gas sensor for carbon dioxide detection at room temperature. *Sens. Actuators, B* **2010**, *149*, 368−372.

(43) Patil, D. R.; Patil, L. A. Cr₂O₃ -modified ZnO thick film resistors as LPG sensors. *Talanta* **2009**, *77*, 1409−1414.

(44) Jain, K.; Pant, R. P.; Lakshmikumar, S. T. Effect of Ni doping on thick film SnO₂ gas sensor. *Sens. Actuators, B* **2006**, *113*, 823−829.

(45) Fu, Y.; Su, Y. S.; Manthiram, A. Sulfur-polypyrrole composite cathodes for lithiumsulfur batteries. *J. Electrochem. Soc.* **2012**, *159*, A1420.

(46) Kumar, P. R.; Maharajan, T. M.; Chinnasamy, M.; Pitchiah, A.; Prabu, J.; Kumar, K. S. Hydroxyl radical scavenging activity of La2O3 nanoparticles. *Pharma Innovation* **2019**, *8*, 759−763.

(47) Abtmeyer, S.; Pązik, R.; Wiglusz, R. J.; Małecka, M.; Seisenbaeva, G. A.; Kessler, V. G. Lanthanum molybdate nano-particles from the Bradley reaction: factors influencing their composition, structure, and functional characteristics as potential matrixes for luminescent phosphors. *Inorg. Chem.* **2014**, *53*, 943−951.

(48) Fatema, K. N.; Sagadevan, S.; Liu, Y.; Cho, K. Y.; Jung, C. H.; Oh, W. C. New design of mesoporous SiO₂ combined In2O3-graphene semiconductor nanocomposite for highly effective and selective gas detection. *J. Mater. Sci.* **2020**, *55*, 13085−13101.

(49) Xia, Z. Y.; Pezzini, S.; Treossi, E.; Giambastiani, G.; Corticelli, F.; Morandi, V.; Zanelli, A.; Bellani, V.; Palermo, V. The exfoliation of graphene in liquids by electrochemical, chemical, and sonication-assisted techniques: a nanoscale study. *Adv. Funct. Mater.* **2013**, *23*, 4684−4693.

(50) Karim, M. R.; Rahman, M. M.; Asiri, A. M.; Hayami, S. Branched alkylamine−reduced graphene oxide hybrids as a dual proton− electron conductor and organic-only water-splitting photo-catalyst. *ACS Appl. Mater. Interfaces* **2020**, *12*, 10829−10838.

(51) Rafat, M. N.; Cho, K. Y.; Jung, C. H.; Oh, W. C. New modeling of 3D quaternary type BaCuZnS-graphene-TiO₂ (BCZS-G-T) composite for photosonocatalytic hydrogen evolution with scavenger effect. *Photochem. Photobiol. Sci.* **2020**, *19*, 1765.

(52) Xiong, E.; Yan, X.; Zhang, X.; Li, Y.; Yang, R.; Meng, L.; Chen, J. A new photoelectrochemical biosensor for ultrasensitive determination of nucleic acids based on a three-stage cascade signal amplification strategy. *Analyst* **2018**, *143*, 2799−2806.

(53) Fatema, K. N.; Jung, C. H.; Liu, Y.; Sagadevan, S.; Cho, K. Y.; Oh, W. C. New design of active material based on YInWO₄-G-SiO₂ for a urea sensor and high performance for nonenzymatic electrical sensitivity. *ACS Biomater. Sci. Eng.* **2020**, *6*, 6981−6994.

(54) Jha, R. K.; D'Costa, J. V.; Sakhuja, N.; Bhat, N. MoSe₂ nanoflakes based chemiresistive sensors for ppb-level hydrogen sulfide gas detection. *Sens. Actuators, B* **2019**, *297*, 126687.

(55) Ravindra, N. M.; Tang, W.; Rassay, S. Transition metal dichalcogenides properties and applications. *Semiconductors*; Springer: Cham, 2019; pp 333−396.

(56) Jha, R. K.; Bhat, N. Recent progress in chemiresistive gas sensing technology based on molybdenum and tungsten chalcogenide nanostructures. *Adv. Mater. Interfac.* **2020**, *7*, 1901992.

(57) Biswas, M. R. U. D.; Oh, W. C. A Review on Sensing and Functional Applications of Graphene-polymer Nanocomposites. *J. Multifunct. Mater. Photoscience* **2018**, *9*, 49−113.

(58) Ji, H.; Zeng, W.; Li, Y. Gas sensing mechanisms of metal oxide semiconductors: a focus review. *Nanoscale* **2019**, *11*, 22664−22684.

(59) Zhang, D.; Yang, Z.; Yu, S.; Mi, Q.; Pan, Q. Diversiform metal oxide-based hybrid nanostructures for gas sensing with versatile prospects. *Coord. Chem.* **2020**, *413*, 213272.

(60) Wang, D.; Zhang, D.; Yang, Y.; Mi, Q.; Zhang, J.; Yu, L. Multifunctional latex/polytetrafluoroethylene-based triboelectric nanogenerator for self-powered organ-like MXene/metal−organic

framework-derived CuO nanohybrid ammonia sensor. *ACS Nano* **2021**, *15*, 2911−2919.